2. E. D. Humphreys and R. W. Clayton, *J. Geophys. Res.* **95**, 19725 (1990).
3. P. Bird and R. W. Rosenstock, *Geol. Soc. Am. Bull.* **95**, 946 (1984).
4. E. D. Humphreys and B. H. Hager, *J. Geophys. Res.* **95**, 19747 (1990).
5. B. Sheffels and M. McNutt, *ibid.* **91**, 6419 (1986).
6. D. Hadley and H. Kanamori, *Geol. Soc. Am. Bull.* **88**, 1469 (1977).
7. R. S. Yeats, *J. Geophys. Res.* **88**, 569 (1983); E. Hauksson and L. M. Hones, *ibid.* **94**, 9569 (1989); T. L. Davis, J. Namson, R. F. Yerkes, *ibid.*, p. 9644.
8. J. Revenaugh, *Geophys. Res. Lett.* **22**, 543 (1995).
9. First arrivals (teleseismic *P* waves) of all records are aligned on t_0. This eliminates delays accrued before entry into the study area and from shallow structure beneath stations.
10. Travel times are based on the IASP91 model of B. L. N. Kennett, in *International Association of Seismology and Physics of the Earth's Interior (IASPEI) 1991 Seismological Tables*, B. L. N. Kennett, Ed. (Research School of Earth Sciences, Australian National University, Canberra, 1991). Velocity heterogeneity dephases scattered energy, resulting in lowered stack amplitudes; the use of unsigned data and running means partially alleviates phase incoherence but reduces resolution.
11. *N*th-root stacking is discussed in P. L. McFadden, B. J. Drummond, S. Kravis, *Geophysics* **51**, 1879 (1986). Linear stacking has $n = 1$; higher values of n result in better suppression of incoherent energy. I use sixth-root stacking ($n = 6$), but results are stable for $1 \leq n \leq 8$.
12. This is not a true bootstrap, which would approximate the distribution of observed $S(\mathbf{x})$; although that is not without interest, I am most concerned with the significance of scatterer detection that necessitates estimation of the distribution of $S(\mathbf{x})$ in the absence of scattered energy. At each migration point 1000 bootstrap iterations were performed.
13. Finite source duration and source-side scattering are treated by deconvolution of a generalized source-time function obtained from a linear stack of all stations that recorded the event. The bootstrap includes station-side reverberations due to coherent crustal reflections and basin resonances, minimizing their effects on scattering potential.
14. Synthetic tests of linear arrays of point scatterers at these depths reveal a tendency of KCM to extend scattering beyond its true spatial terminus and to warp the ends down or up depending on location within the SCSN, explaining the "frowns" outside the range 119° to 116°W. See Fig. 3.
15. C. H. Jones, H. Kanamori, S. W. Roecker, *J. Geophys. Res.* **99**, 4567 (1994).
16. This conclusion is reached on the combined basis of: (i) success of the isotropic scattering model (highly directional or very low-angle scattering would be strongly damped); (ii) consistency of results over a range of scattering angles; and (iii) temporal localization of energy on the seismogram (Eq. 2 sums less than 1 s of data per seismogram per scatterer), all of which are consistent with $ka \ll 1$; K. Aki and P. G. Richards, *Quantitative Seismology* (Freeman, San Francisco, 1980).
17. A period of 2×10^6 years is less than half the duration of subduction (*4*); thus, the predicted width of the boundary layer is a lower bound favoring scattering.
18. Scattering from planar contacts within the slab also occurs but is minor because the radiation pattern is highly directional.
19. Although it is not possible to directly estimate absolute scattering strength from nonlinear stacks, forward modeling suggests that slab-induced *P* to *P* single scattering accounts for only a very small fraction of coda energy, probably less than 5%. Shallow *P* to *P* and *P* to *S* scattering, *P* to *Rg* scattering near the free surface, and multiple scattering comprise most of the *P*-wave coda.
20. I thank E. Humphreys and an anonymous reviewer for helpful comments and suggestions. This research was supported by the National Science Foundation. Lunchtime Software Guild contribution 13.

18 January 1995; accepted 11 April 1995

Structure and Density of FeS at High Pressure and High Temperature and the Internal Structure of Mars

Yingwei Fei, Charles T. Prewitt, Ho-kwang Mao,
Constance M. Bertka

In situ x-ray diffraction measurements revealed that FeS, a possible core material for the terrestrial planets, transforms to a hexagonal NiAs superstructure with axial ratio (*c/a*) close to the ideal close-packing value of 1.63 at high pressure and high temperature. The high-pressure-temperature phase has shorter Fe-Fe distances than the low-pressure phase. Significant shortening of the Fe-Fe distance would lead to metallization of FeS, resulting in fundamental changes in physical properties of FeS at high pressure and temperature. Calculations using the density of the high-pressure-temperature FeS phase indicate that the martian core-mantle boundary occurs within the silicate perovskite stability field.

Iron sulfide (FeS) has been found in many meteorites and is believed to be a possible component of the cores of terrestrial planets such as Earth and Mars. Models of internal structure of the planets with sulfur-bearing cores require accurate determinations of phase relations and densities of FeS at high pressure and high temperature, but study has been difficult because it has not proven possible to quench the high-pressure-temperature phases. Previously, phase transitions in FeS have been investigated only at high pressure and room temperature (*1–5*) and at high temperature and ambient pressure (*6*, *7*). We have developed techniques for determining the structure and density of materials under simultaneous high pressure and temperature conditions (*8*). In this study, we report the structure and density of FeS at high pressure and high temperature. We then use these data to evaluate the relation between the depth of the martian core-mantle boundary and the sulfur content of the core.

Stoichiometric FeS at ambient conditions, called troilite (FeS I), has a NiAs-type hexagonal structure with a ($\sqrt{3}a$, $2c$) unit cell. Troilite transforms to a MnP-type structure (FeS II) at 3.4 GPa (*5*). A high-pressure phase (FeS III) forms at pressures above 6.7 GPa (*1*, *3*), although its structure is uncertain (*9*). We conducted in situ synchrotron x-ray diffraction measurements on FeS using an externally heated diamond-anvil cell with the sample loaded in a hydrostatic Ne pressure medium (*10*). At 300 K, we confirmed the two previously observed phase transitions. Upon heating the FeS sample at high pressures (>6.7 GPa), we observed a different x-ray diffraction pattern (Fig. 1). The diffraction pattern is much simpler than that of the high-pressure phase (FeS III) and can be indexed on a hexagonal cell. The calculated x-ray diffraction pattern, based on a NiAs-type hexagonal structure with a ($2a$, c) unit cell, agrees well with the observed data (Table 1). The experimental data demonstrate that this high-pressure-temperature phase, which we named FeS IV, has a NiAs-type superstructure lattice, in which the hexagonal layers of Fe and S are alternately stacked along the *c* axis and the Fe atoms are slightly displaced such that a perfectly repeating unit cell occurs by doubling the *a* distance. The axial ratio (*c/a*) of FeS IV is close to an ideal close-packing value of 1.63. The phase boundary of the FeS III–FeS IV transition (Fig. 2) was determined to be $P = -11.25 + 0.0485T$ (for pressure P in gigapascals and temperature T in kelvin). By analyzing the x-ray diffraction data, we also obtained the density of FeS IV as a function of pressure at high temperatures (Fig. 3A).

A high-temperature phase of FeS has also been observed at about 420 K and ambient pressure (*6*, *7*). The structure of this high-temperature phase has been controversial (*5*, *7*) because of a discrepancy resulting from the assumption that the high-temperature phase has the same structure as the intermediate high-pressure phase (FeS II). Our experimental data show that the high-temperature phase has a hexagonal structure with a ($2a$, c) unit cell, as reported by Keller-Besrest and Collin (*7*), and that the structure of the intermediate high-pressure phase (FeS II) is consistent with the MnP-type structure reported by King and Prewitt (*5*). The high-tempera-

---

Geophysical Laboratory and Center for High Pressure Research, Carnegie Institution of Washington, 5251 Broad Branch Road, NW, Washington, DC 20015, USA.

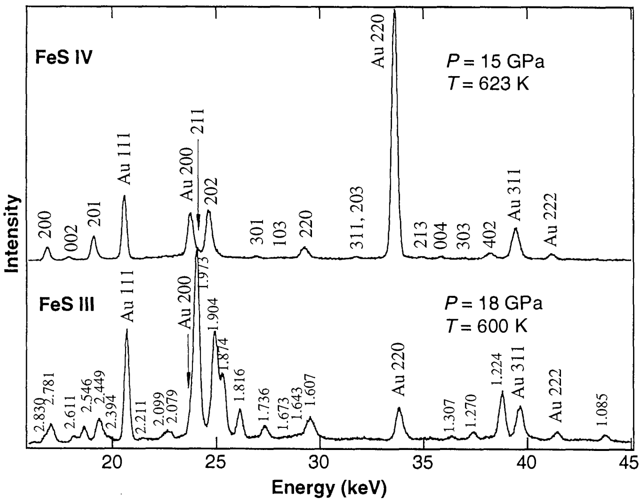

Fig. 1. Energy-dispersive x-ray diffraction spectra of the high-pressure-temperature phase of FeS (FeS IV) (upper spectrum) and the high-pressure phase (FeS III) (lower spectrum). The diffraction pattern of FeS IV was indexed with a hexagonal cell (Table 1). The *hkl* indices are indicated for each diffraction peak. The peak positions for FeS III are indicated by the interplanar *d* spacing in angstroms.

ture phase has the same structure as the high-pressure-temperature phase FeS IV, but the high-pressure-temperature phase has much more efficient packing than the high-temperature phase, as reflected in the variation of *c*/*a* versus pressure (Fig. 3B). The decrease in the *c*/*a* ratio at about 6 GPa results from the change of the *c* parameter from 5.70 to 5.54 Å. This abrupt shortening of the *c* axis results in a density change of about 4%. The densification must result from an electronic transition, possibly a spin-pairing transition, because no structure transition was observed. A change in the electronic structure of Fe in FeS at a similar pressure was also indicated by King *et al.* (*3*) on the basis of a Mössbauer spectroscopic study. The *c*-axis shortening across the electronic transition means that the high-pressure-temperature phase has substantially shorter interlayer Fe-Fe distances, which would lead to metallization of FeS at high pressure.

Upon further heating at low pressures (<10 GPa), the NiAs-type hexagonal structure with a (2*a*, *c*) unit cell, FeS IV, transformed to a simple NiAs-type structure with a (*a*, *c*) unit cell (FeS V) (Fig. 2). The nonlinear phase boundary between the phases IV and V can be understood from energetic change as a function of density. The change in the temperature-pressure slope of the transition reflects the densification across the electronic transition at about 6 GPa.

Our experimental results have direct applications to the internal structure of Mars because the experimental pressure-temperature ranges are comparable to those of the interior of Mars (Fig. 2). On the basis of cosmochemical constraints and the thermal history of the planet, the iron-dominant martian core may be as much as 34% sulfur by weight (*11*) (corresponding approximately to stoichiometric FeS). Because of the lack of seismic data, calculations of the martian core-mantle boundary must depend on the value assumed for the core density. Previous calculations (*11–14*) suggested that the depth of the martian core-mantle boundary is 1370 to 1990 km, depending on the sulfur content of the core. However, these calculations were based on the density data for the high-pressure phase FeS III (*4*, *15*), whose structure has not yet been definitely determined. Our experiments indicate that all of these calculations of density for a FeS martian core were based on the wrong polymorph of FeS. The stable FeS polymorph at martian core pressures and temperatures is a hexagonal NiAs superstructure (FeS IV). Our calculated depth of the martian core-mantle boundary is about 1720 km (approximately corresponding to pressure of 20 GPa) for the

Table 1. Observed and calculated x-ray diffraction pattern of FeS IV at 15 GPa and 623 K. The interplanar spacings *d* are given in angstroms; *hkl* are the Miller indices.

h	*k*	*l*	d_{obs}	d_{cal}*	Δd
2	0	0	2.811	2.811	0.000
0	0	2	2.649	2.650	−0.001
2	0	1	2.483	2.483	0.000
2	1	1	1.978	1.972	0.006
2	0	2	1.928	1.928	0.000
3	0	1	1.761	1.767	−0.006
1	0	3	1.684	1.686	−0.002
2	2	0	1.622	1.623	−0.001
2	0	3	1.495	1.496	−0.001
3	1	1	1.495	1.496	−0.001
2	1	3	1.359	1.359	0.000
0	0	4	1.325	1.325	0.000
3	0	3	1.288	1.286	0.002
4	0	2	1.242	1.242	0.000

*Hexagonal NiAs superstructure with (2*a*, *c*) unit cell: *a* = 3.246(2) Å and *c* = 5.301 (2) Å, which gives *c*/*a* = 1.633. The observed intensities for the diffraction pattern are shown in Fig. 1. Preferred orientation effects in the patterns collected at different pressures and temperatures were observed.

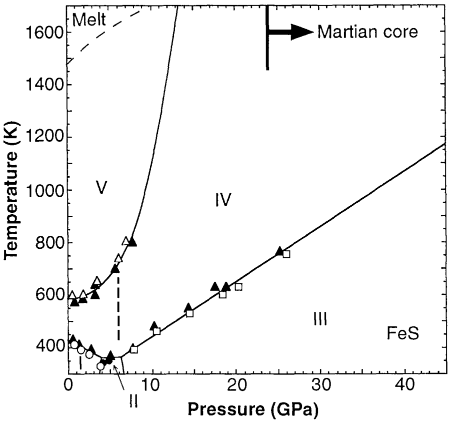

Fig. 2. Experimentally determined phase diagram of FeS. Experimental data (reported only near the phase boundary) are represented by symbols. (○) FeS I, NiAs-type structure with a ($\sqrt{3}a$, 2*c*) unit cell; (●) FeS II, MnP-type structure; (□) FeS III, monoclinic?; (▲) FeS IV, NiAs-type structure with a (2*a*, *c*) unit cell; (△) FeS V, NiAs-type structure with a (*a*, *c*) unit cell. The thick dashed line indicates the electronic transition in the stability field of FeS IV.

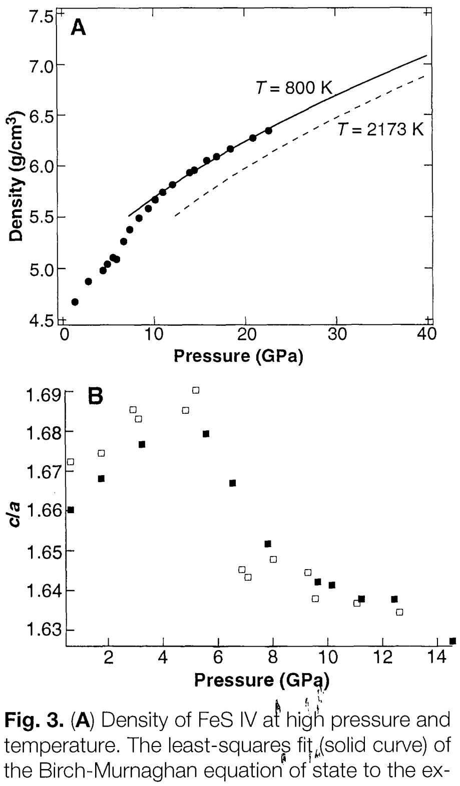

Fig. 3. (**A**) Density of FeS IV at high pressure and temperature. The least-squares fit (solid curve) of the Birch-Murnaghan equation of state to the experimental data at 800 K (●) yielded a zero-pressure density $\rho_0 = 4.94 \pm 0.05$ g/cm^3 and isothermal bulk modulus $K_T = 54 \pm 6$ GPa with its pressure derivative $(\partial K_T/\partial P)_T = 4$. Density data below and near the transition pressure were not used in the fit. Densities at 2173 K (dashed curve) were calculated by using the thermal pressure $P_{th} = P_{800K} + \alpha K_T(T - 800)$, where $\alpha K_T = 3.7 \times 10^{-3}$ GPa/K. (**B**) The abrupt change in the *c*/*a* ratio of FeS IV along isothermal compression curves at (□) 500 K and (■) 600 K.

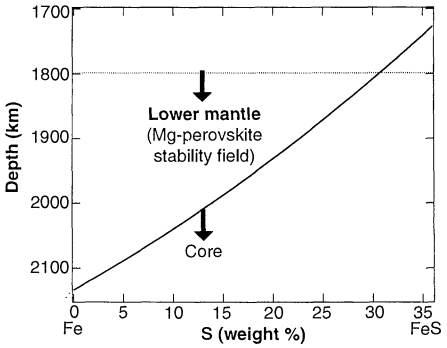

Fig. 4. Calculated relation between the depth of the martian core-mantle boundary and the sulfur content, based on our experimentally determined density data for FeS IV. Dashed line indicates the depth of Mg–silicate perovskite stability.

pure FeS core (*16*), deeper than previous calculations (*11, 14*). The reason for this difference is that FeS IV is much more compressible than earlier assumed. For a model mantle composition of Mars (*12*) with 13.9 weight % sulfur in the core, the martian core-mantle boundary is located at a depth of 2000 km (about 24 GPa), deeper than the silicate perovskite stability field. A core with at least 30 weight % sulfur is required to eliminate a silicate perovskite lower mantle in Mars (Fig. 4). In comparison with the internal structure of the Earth, Mars may have only a thin layer of lower mantle (~200 km) but similar density discontinuities.

Melting relations in the Fe-FeS system have been used to constrain the temperatures of the interior of planets in many planetary models (*17*). The discovery of the transformation of the high-pressure phase FeS III to the high-pressure-temperature hexagonal phase FeS IV has a significant impact on the understanding of melting relations in the FeS and Fe-FeS systems and of solution behavior in systems such as Fe-S-O at high pressure and temperature. Changes in the physical properties of FeS at high pressure and temperature, such as density and chemical bonding, will lead to changes in melting temperatures and melting behavior in binary (for example, Fe-S) or ternary (for example, Fe-S-O) systems. These changes also have profound implications for the incorporation of lighter elements into iron-dominant cores of terrestrial planets (*18*).

REFERENCES AND NOTES

1. L. A. Taylor and H. K. Mao, *Science* **170**, 850 (1970).
2. R. O. Pichulo, J. S. Weaver, T. Takahashi, *Meteoritics* **11**, 351 (1976).
3. H. E. Jr. King, D. Virgo, H. K. Mao, *Carnegie Inst. Washington Yearb.* **77**, 830 (1978).
4. H. K. Mao, G. Zou, P. B. Bell, *ibid.* **80**, 267 (1981).
5. H. E. Jr. King and C. T. Prewitt, *Acta Crystallogr. B* **38**, 1877 (1982).
6. L. A. Taylor, *Carnegie Inst. Washington Yearb.* **68**, 259 (1970); A. Putnis, *Science* **186**, 439 (1974); G. Collin, M. F. Gardette, R. Comes, *J. Phys. Chem. Solids* **48**, 791 (1987).
7. F. Keller-Besrest and G. Collin, *J. Solid State Chem.* **84**, 194 (1990).
8. Y. Fei, H. K. Mao, J. Shu, J. Hu, *Phys. Chem. Miner.* **18**, 416 (1992).
9. C. T. Prewitt and Y. Fei, paper presented at the 16th International Mineralogy Association Meeting, Pisa, Italy, 4 September 1994. Even with high-quality synchrotron x-ray data, it has been difficult to determine the symmetry of FeS III because diffraction patterns from different experiments are not consistent with each other, probably because of preferred orientation effects. However, it has been possible to index peaks that occur consistently in x-ray patterns at several different pressures on a monoclinic cell with a = 5.121(2) Å, b = 5.577(2) Å, c = 3.328(2) Å, and β = 95.95(4)° at 15 GPa (the numbers in parentheses are the errors in the last digits). The structure seems to still be related to that of NiAs but with significant distortions of the simple NiAs structure.
10. Experimental configuration for high-pressure and high-temperature experiments in a diamond-anvil cell, combined with synchrotron x-ray diffraction techniques, was described in (*8*). The FeS samples were synthesized from a mixture of iron and sulfur, sealed in evacuated silica glass tube, and heated for 4 days at 700°C. The starting materials were stoichiometric FeS, confirmed by electron microprobe analyses and x-ray diffraction.
11. Basaltic Volcanism Study Project (BVSP), *Basaltic Volcanism on the Terrestrial Planets* (Pergamon, New York, 1981); J. Longhi, E. Knittle, J. R. Holloway, H. Wänke, in *Mars*, H. H. Kieffer, B. M. Jakosky, C. W. Snyder, M. S. Matthews, Eds. (Univ. of Arizona Press, Tucson, 1992), pp. 184–208.
12. J. W. Morgan and E. Anders, *Geochim. Cosmochim. Acta* **43**, 1601 (1979).
13. H. Wänke and G. Dreibus, *Philos. Trans. R. Soc. London A* **235**, 545 (1988); T. R. McGetchin and J. R. Smyth, *Icarus* **34**, 512 (1978).
14. E. Ohtani and N. Kamaya, *Geophys. Res. Lett.* **19**, 2239 (1992).
15. T. J. Ahrens, *J. Geophys. Res.* **84**, 985 (1979); J. M. Brown, T. J. Ahrens, D. L. Shampine, *ibid.* **89**, 6041 (1984).
16. The depth of the martian core-mantle boundary was calculated by satisfying simultaneously the mass and a moment of inertia factor of the planet [G. Schubert and T. Spohn, *ibid.* **95**, 14095 (1990)] based on density profiles of the mantle (*14*) and the core. The geotherm for Mars used in the calculations is from D. H. Johnston and M. N. Toksöz [*Icarus* **32**, 73 (1977)]. Densities for the pure Fe core were calculated with compression parameters (*14*) and the thermal expansivity data [R. Boehler, N. Bargen, A. Chopelas, *J. Geophys. Res.* **95**, 21731 (1990)] of face-centered-cubic iron. Densities for the pure FeS core were from our experimental determination (Fig. 3). The density profiles used in our calculations are best fit to a moment of inertia factor of 0.367.
17. F. Birch, *J. Geophys. Res.* **69**, 4377 (1964); B. Mason, *Nature* **211**, 616 (1966); V. R. Murthy and H. T. Hall, *Phys. Earth Planet. Inter.* **2**, 276 (1970); Q. Williams and R. Jeanloz, *J. Geophys. Res.* **95**, 19299 (1990); R. Boehler, *Earth Planet. Sci. Lett.* **111**, 217 (1992).
18. Y. Fei and H. K. Mao, *Science* **266**, 1678 (1994).
19. We thank J. Hu for experimental assistance. Supported by the National Science Foundation Center for High-Pressure Research, the National Aeronautics and Space Administration, and the Carnegie Institution of Washington.

9 January 1995; accepted 1 May 1995

Managing the Evolution of Insect Resistance to Transgenic Plants

D. N. Alstad* and D. A. Andow

The evolution of resistance in pests such as the European corn borer will imperil transgenic maize varieties that express insecticidal crystal proteins of *Bacillus thuringiensis*. Patchworks of treated and untreated fields can delay the evolution of pesticide resistance, but the untreated refuge fields are likely to sustain heavy damage. A strategy that exploits corn borer preferences and movements can eliminate this problem. Computer simulation indicates that this approach can delay the evolution of resistance and reduce insect damage in the untreated fields of a patchwork planting regime.

Maize, cotton, potatoes, and tobacco have now been genetically engineered to express crystal protein (*cry*) genes from *Bacillus thuringiensis*. Maize varieties nearing commercialization are toxic to many Lepidoptera, including *Ostrinia nubilalis* (Hübner) [Pyralidae], the European corn borer, one of the most injurious pests of maize in North America. A potential problem with genetically engineered crop varieties is the evolution of resistance in target pests (*1*).

Insect resistance to transgenic plants has much in common with resistance to pesticides. Potential management strategies against pesticide resistance include the application of multiple toxins in mixtures or sequences (*2, 3*), the use of high toxin concentrations to make expression of the resistance alleles more recessive (*3–5*), and the distribution of the toxin in spatial patches interspersed with nontoxic refuges. Because the efficacy of toxin mixtures remains controversial, discussion of resistance management in transgenic crops has focused on the relative merits of the "high-dose" strategy and spatial refuges (*2–6*).

Comins and others (*3–6*) have shown that random gene exchange between select-

---

D. N. Alstad, Department of Ecology, Evolution, and Behavior and Center for Community Genetics, University of Minnesota, St. Paul, MN 55108-6097, USA. E-mail: dna@ecology.umn.edu
D. A. Andow, Department of Entomology and Center for Community Genetics, University of Minnesota, St. Paul, MN 55108, USA.

*To whom correspondence should be addressed.